crystals

MDPI

Article

Numerical Investigation into the Influence of Grain Orientation Distribution on the Local and Global Elastic-Plastic Behaviour of Polycrystalline Nickel-Based Superalloy INC-738 LC

Benedikt Engel *, Mark Huth and Christopher Hyde

Gas Turbine and Transmissions Research Centre (G2TRC), University of Nottingham, Nottingham NG7 2RD, UK;
ezymah@exmail.nottingham.ac.uk (M.H.); christopher.hyde@nottingham.ac.uk (C.H.)
* Correspondence: benedikt.engel@nottingham.ac.uk

Abstract: Polycrystalline nickel-based superalloys tend to have large grains within component areas where high loads are dominant during operation. Due to these large grains, caused by the manufacturing and cooling process, the orientation of each grain becomes highly important, since it influences the elastic and plastic behaviour of the material. With the usage of the open source codes NEPER and FEPX, polycrystalline models of Inconel 738 LC were generated and their elastic and crystal plasticity behaviour simulated in dependence of different orientation distributions under uniaxial loading. Orientation distributions close to the [100] direction showed the lowest Young's moduli as well as the highest elastic strains before yielding, as expected. Orientations close to the [$\bar{5}$89] direction, showed the lowest elastic strains and therefore first plastic deformation under strain loading due to the highest shear stress in the slip systems caused by the interaction of Young's modulus and the Schmid factor.

Keywords: nickel-based superalloy; anisotropy; slip system modelling; Schmid factor; Young's moduli

Citation: Engel, B.; Huth, M.; Hyde, C. Numerical Investigation into the Influence of Grain Orientation Distribution on the Local and Global Elastic-Plastic Behaviour of Polycrystalline Nickel-Based Superalloy INC-738 LC. *Crystals* **2022**, *12*, x. https://doi.org/10.3390/xxxxx

Academic Editor: Wojciech Polkowski

Received: 24 December 2021
Accepted: 11 January 2022
Published:

Publisher's Note: MDPI stays neutral with regard to jurisdictional claims in published maps and institutional affiliations.

1. Introduction

Stationary gas turbines, as used in gas power plants, can be started from cold to a maximum output in less than 30 min [1]. Due to this short start-up time, gas power plants are able to react to shortages in the electricity supply caused by volatile feed in of renewables energies and can stabilize the electricity grid in times of high demand. Due to frequent start-up, shut down and load changes, the components in the hot gas section, especially the turbine blades and vanes undergo high mechanical and thermal loads, which has to be considered in the design process. Current design paradigms are based on deterministic lifetime approaches, which lead to conservative designs and inefficient component geometries caused by high safety factors. In recent years, these deterministic approaches were successfully replaced by probabilistic approaches, which are based on the statistical distribution of factors, which affects the high temperature fatigue life of the considered materials [2–4].

Polycrystalline nickel-based superalloys are widely used in the rear hot gas section as blades and vanes. Due to the casting manufacturing process and the component geometries, large grains with diameters up to 3–4 mm can form in areas where high loads appear during operations. Experimental strain controlled high temperature fatigue tests of nickel-base superalloys with large grains, i.e., low grain numbers in the gauge sections, show significantly large scatter in the lifetime as well as in the mechanical properties. As

shown by several authors, the scatter in fatigue life and mechanical properties can be mainly attributed to two characteristics, the local grain orientation and the low amount of grains. Nickel-based superalloys show a high elastic anisotropy factors up to 2.7 [5]; therefore, the local orientation distribution of the grains within the gauge section have a significant influence on the elastic response of the component. This leads, in combination with the low amount of grains, to a non-averaging of mechanical properties as known for isotropic materials. For example, some austenitic steels show higher elastic anisotropies [6,7], but due to significantly smaller grains known for stainless steels, mechanical properties are averaging over the high amount of grains, and the macroscopic material behaviour can be classified as isotropic.

Furthermore, the local grain orientation influences the local plastic behaviour. If a critical shear stress within the slip systems of the grain is exceeded, dislocations start moving within the slip systems, which represents plastic deformation. For a face-centred crystal structure (fcc), such as nickel, slip mainly occurs preferably in one of the 12 slip systems of the type {111}<110>, which are composed of four closed packed planes together with three close packed directions. As proposed by Schmid [8], the resulting shear stress within a slip system can be calculated by the product of the cosines of slip system direction and slip system plane (the so-called Schmid factor m) related to the loading direction and the applied normal load. Numerical investigations showed for 100,000 randomly orientated fcc single crystals, the minimum possible Schmid factor under normal loading is 0.28, which occurs only with a probability of 0.032 %. The highest and also most frequently occurring Schmid factor is 0.5, which occurs with a probability of 16.4 %. On average, the Schmid factor is calculated to 0.45 ± 0.041 for a single grain under uniaxial loading [9]. Seibel, Schmitz et al. [10,11] could significantly decrease the occurring scatter in a total strain Wöhler diagram for polycrystalline nickel-based superalloy Rene80, by determining the Schmid factor of the crack initiating grains using electron backscatter diffraction (EBSD), estimating the resulting shear stress and representing it over the lifetime. Further experimental and analytical investigations showed that with the usage of the product of the Young's moduli (E) and the Schmid factor (m) the so-called E·m value, predictions can be made in which grains plastic deformations concentrates. These grains tends to form persistent slip bands and provide crack initiations as shown in [12]. With the usage of polycrystalline finite element models and calculations of resulting shear stresses within the slip system, it could be proven that different orientation distribution within the materials can lead to improvements of the mechanical properties [13]. For smooth specimen made of random orientated coarse grain nickel-based superalloy Rene80 Young's moduli were in general higher compared to smooth specimen made from the same material batch but with a determined crystallographic texture (resulting from the casting process). In addition to lower Young's moduli and therefore lower stresses for tests under total strain control (compared to the random orientated material), the texture of the grains also leads to a shift of the Schmid factor distribution to lower values. This leads to lower resulting shear stresses in the slip systems and therefore to a delay in crack initiation and therefore longer lifetimes. Based on these findings, a probabilistic lifetime models for both variants of the material could be developed with a great accordance to observed experimental results. The same material batch, as discussed before, was investigated in [14] but for notched specimen. Contrary to all expectations, the material with the crystallographic texture didn't show any improvements in lifetime or mechanical properties. This can be attributed to the interaction of varying stress states along the notch with the crystallographic texture, which lead to high stiffness along the notch area, which increases the local stresses and shear stresses [15].

All above mentioned numerical researches were conducted using anisotropic elastic material models were calculated up to the point where the elastic resulting shear stress within the slip systems reaches a critical value and plastic deformation starts. The following paper investigates how local grain orientation also affects the plastic behaviour of polycrystalline nickel-based superalloys by numerical simulation. Specifically, the influence

of different orientation distributions on the local and global onset of plasticity as well as the interaction of grains will be investigated.

2. Materials and Methods

2.1. Material

The investigated material is the polycrystalline nickel-based superalloy IN-738 LC, which has the composition shown in Table 1.

Table 1. Composition of IN-738LC [16].

Element	Ni	Cr	Co	Ti	Al	W	Mo	Ta	C	Nb
Wt.%	Bal.	16	8.58	3.42	3.36	2.67	1.81	1.9	0.105	0.9

This material is a precipitation strengthened nickel-based superalloy with around 59 vol.% of cuboid shaped γ′ embedded in the γ matrix with grain sizes up to 3 mm in dependence of the manufacturing process and specimen design [17,18].

2.2. Material Modelling

Finite element simulations were carried out for polycrystalline models by using the open source codes NEPER (Version 4, by Romain Quey, MINES Saint-Étienne) [19,20] and FEPX (Version 1.1.2 by Paul Dawson, Cornell University) [21]. Neper is able to generate complex geometric components made of polycrystals by using three dimensional Voronoi tessellation and allows for a convenient meshing procedure. The generated model file can be exported as an input file for commercial finite element solvers or passed on to FEPX. FEPX is a finite element solver that allows for elastic and plastic calculations within polycrystals under the assumption of crystallographic characteristics within the material (i.e., slip system, anisotropy effects) to be performed. The main advantage of FEPX is the large range of possible material properties that can be considered. For example, FEPX includes non-linear kinematic hardening, rate-dependent slip within the slip systems, the evolution of state variables for crystal lattice orientation and slip system strength. In the following the main equations, which are important in this work, will be discussed where further details can be found in [21].

The elastic regime of the material in dependence of its orientation will be described by using a generalized Hooke's law for cubic crystals. The stress tensor $\underline{C}$ can be calculated by using the stiffness tensor $\underline{C}$, with the material constants C_{11}, C_{12} and C_{44}, multiplied by the elastic strain ε according to Equation (1).

$$\boldsymbol{\sigma} = \underline{\boldsymbol{C}}\boldsymbol{\varepsilon} \tag{1}$$

Grains within polycrystalline materials are characterized by different grain orientations. In order to calculate the stiffness for a specific grain, the stiffness tensor must be rotated according to the grain orientation related to the loading direction. For plastic deformation, the kinematics of slip are given as a power law function by the following Equation (2).

$$\dot{\boldsymbol{\gamma}}^{\boldsymbol{\alpha}} = \dot{\boldsymbol{\gamma}}_{\mathbf{0}} \left(\frac{|\boldsymbol{\tau}^{\boldsymbol{\alpha}}|}{\boldsymbol{g}^{\boldsymbol{\alpha}}} \right)^{\frac{\mathbf{1}}{\boldsymbol{m}}} \boldsymbol{sgn}(\boldsymbol{\tau}^{\boldsymbol{\alpha}}) \tag{2}$$

With $\dot{\boldsymbol{\gamma}}_{\mathbf{0}}$ the fixed-state strain rate scaling coefficient, $\boldsymbol{\tau}^{\boldsymbol{\alpha}}$ is the resolved shear stress of the $\boldsymbol{\alpha}$th slip system, m is the rate sensitivity coefficient and $\boldsymbol{g}^{\boldsymbol{\alpha}}$ is the current slip system strength or resistance to shear [22]. Note that in FEPX $\boldsymbol{g}^{\boldsymbol{\alpha}}$ is equal for the same family of slip systems. Since $\boldsymbol{g}^{\boldsymbol{\alpha}}$ describes the slip system strength, it can be further varied by using the modified Voce form, to account for cyclic hardening, i.e., slip system strength evolution (Equation (3)).

$$\dot{g^{\alpha}} = h_0 \left(\frac{g_s(\dot{\gamma}) - g^{\alpha}}{g_s(\dot{\gamma}) - g_0} \right)^n g_0 \quad (3)$$

$\boldsymbol{h_0}$ is the fixed-state hardening rate scaling coefficient, $\boldsymbol{g_0}$ is the initial slip system strength (which is considered equal for all slip systems) and n is the non-linear Voce hardening exponent. $\boldsymbol{g_s(\dot{\gamma})}$ describes the slip systems saturation strength and is given by a power law according to Equation (4).

$$g_s(\dot{\gamma}) = g_{s0} \left(\frac{\dot{\gamma}}{\dot{\gamma}_{s0}} \right)^{m'} \quad (4)$$

$\boldsymbol{g_{s0}}$ is the initial slip system saturation strength, $\boldsymbol{m'}$ is the saturation strength rate scaling exponent and $\boldsymbol{\dot{\gamma}_{s0}}$ is the initial saturation slip system shear rate. $\boldsymbol{\dot{\gamma}}$ is the sum of the individual $\boldsymbol{\dot{\gamma^{\alpha}}}$ values. Cyclic hardening [23] is not considered within the present paper.

2.3. Material Parameters

The elastic constants for IN-738 LC [16] were linearly interpolated between the given temperatures of 800 °C and 898 °C to calculate the elastic constants at 850 °C, as given in Table 1.

Table 2. Elastic constants of IN-738 LC at 850 °C.

C_{11}(GPa)	C_{12}(GPa)	C_{44}(GPa)
225.83	161.45	98.79

In order to model the plastic behaviour, IN-738 LC experimental tensile test data (for an assumed random orientation distribution) at 850 °C [24] were fitted and optimized against a model with sufficient amounts of grains for a strain rate of 0.001 s^{-1}. Figure 1 shows the experimental stress-strain data as well as the corresponding fitted elastic plastic material model.

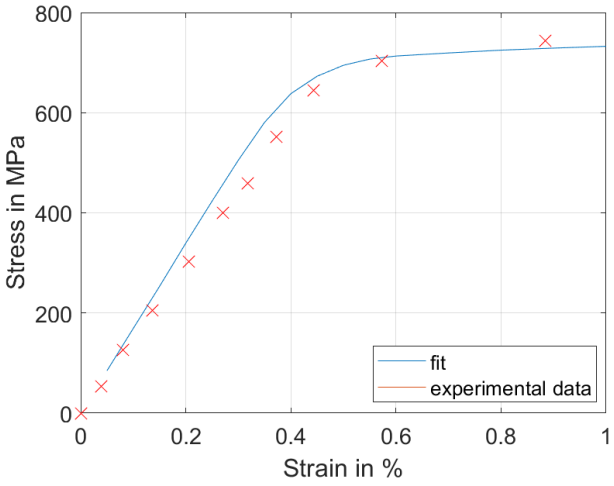

Figure 1. Experimental stress-strain data for IN-738 LC at 850 °C [24] and corresponding fitted elastic plastic polycrystalline model.

Plastic parameters, as shown in Table 2, where derived from the fitting and are used in the following simulations.

Table 2. Fitted plastic constants of IN-738 LC at 850 °C.

$\dot{\gamma}_0$ (s^{-1})	m	h_0(MPa)	g_0(MPa)	n'	g_1(MPa)	$\dot{\gamma}_s(s^{-1})$	m'
1.0	0.05	200	210	1	330	5e10	5e-3

2.4. Simulations

Material behaviour simulations were carried out for a cuboid with a 7 × 7 mm² cross section and 18 mm in length. 49 grains were generated using NEPER, which leads to an average grain size of 3.25 mm in diameter. Figure 2a represents the simulated specimen, within the visualization tool of NEPER.

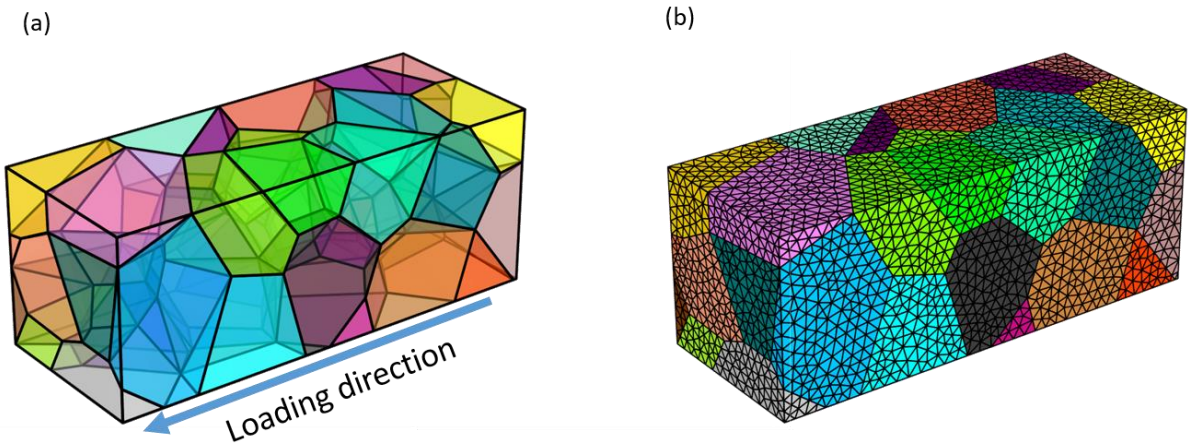

Figure 2. (**a**) Polycrystalline model with 49 grains generated by NEPER and (**b**) meshed equivalent for finite element analysis.

Meshing was conducted using the meshing tool integrated in NEPER, by using a relative cell length value (rcl) of 0.4, which leads to approximately 65000 10-node tetrahedral elements (C3D10), which gives a good compromise between calculation time and accuracy (see Figure 2b). A displacement load in loading direction (see Figure 2a) was applied on one face to ensure a uniaxial loading whereas the other face was locked for rotation and translation. The maximum displacement was set to 0.18 mm, which is the equivalent of 1 % of total strain to allow for distinct plastic deformation. In order to investigate the influence of various orientation distribution, sets of rotational matrices, i.e., Euler angles, were generated and assigned to the grains.

In order to explain the reasons why the following orientation distributions were chosen, the $\boldsymbol{E} \cdot \boldsymbol{m}$ model for a single grain will be explained [9,12]. The main assumption of this model is that the resulting shear stress in a slip system of a single grain under uniaxial strain control is only dependent upon the Young's modulus, E, and Schmid factor, m, of the grain, both of which are defined by the local grain orientation. Under the assumption of an elastic behaviour, the resulting shear stress can be calculated using Equation (5). Note that this equation is only valid up to the point where the resulting shear stress, $\boldsymbol{\tau_{res}}$, is equal to the critical shear stress, $\boldsymbol{\tau_{crit}}$, which is the point at which plastic deformation begins.

$$\boldsymbol{\tau_{res}} = \boldsymbol{\varepsilon_{a,t}} \cdot \boldsymbol{E} \cdot \boldsymbol{m} \tag{5}$$

For a constant total strain, $\boldsymbol{\varepsilon_{a,t}}$, grains with a high value of $\boldsymbol{E} \cdot \boldsymbol{m}$ reach yield earlier compared to grains with low $\boldsymbol{E} \cdot \boldsymbol{m}$ values. The pole figures shown in Figure 3 represent the chosen orientation distributions (see Figure 3a) as well as the value of $\boldsymbol{E} \cdot \boldsymbol{m}$ at 850 °C in dependence of the grain orientation, illustrated as an inverse pole figure (see Figure 3b).

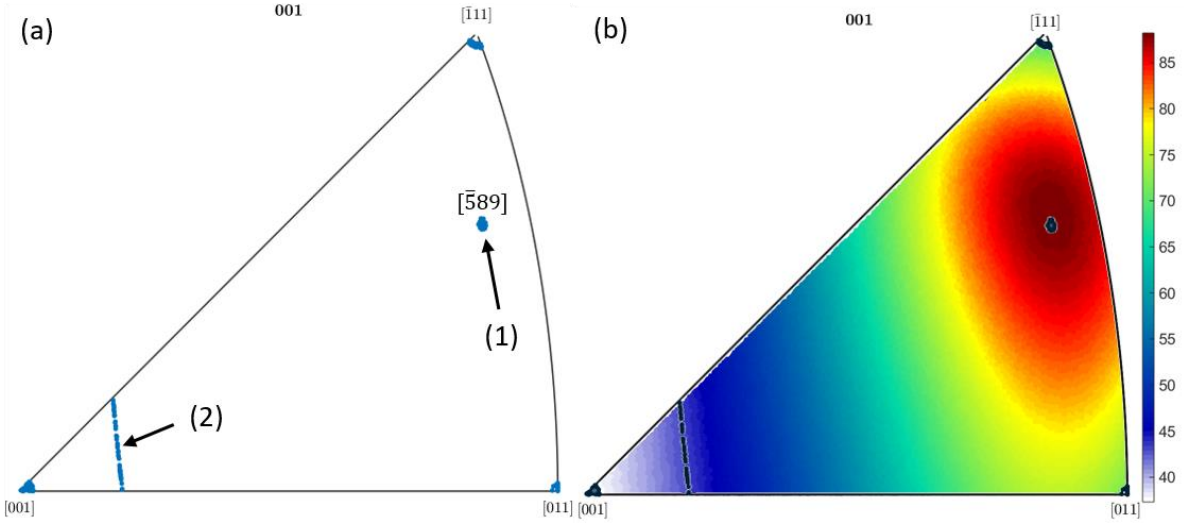

Figure 3. (**a**) Inverse pole figure of chosen grain orientation distributions and (**b**) $\boldsymbol{E} \cdot \boldsymbol{m}$ values at 850 °C.

Whereas the orientations close to [001], [011] and [111] directions will be named the same, orientations at (1) will be considered stiff orientations (close to the [$\bar{5}$89], since they show a maximum in the $\boldsymbol{E} \cdot \boldsymbol{m}$ model (see Figure 3b), whereas (2) will be considered soft, due to the correspondingly low $\boldsymbol{E} \cdot \boldsymbol{m}$ values. Furthermore, six random orientation distribution, were generated in accordance to the Haar measure to ensure statistically random grain orientations [4]. One model is divided in the middle in a half stiff and half soft grain orientation distribution in order to investigate how they interact; this will be considered a mix model.

3. Results

Figure 4 shows the macroscopic stress-strain curves, i.e., the mechanical response of the whole model (see Figure 2) for a uniaxial load in dependence of the different orientation distributions. The yield point is indicated with **x** for each curve whereby it was defined as the point at which the simulated elastic stress (based on the Hooke's law) differs by more than 5 % from the simulated elastic-plastic results.

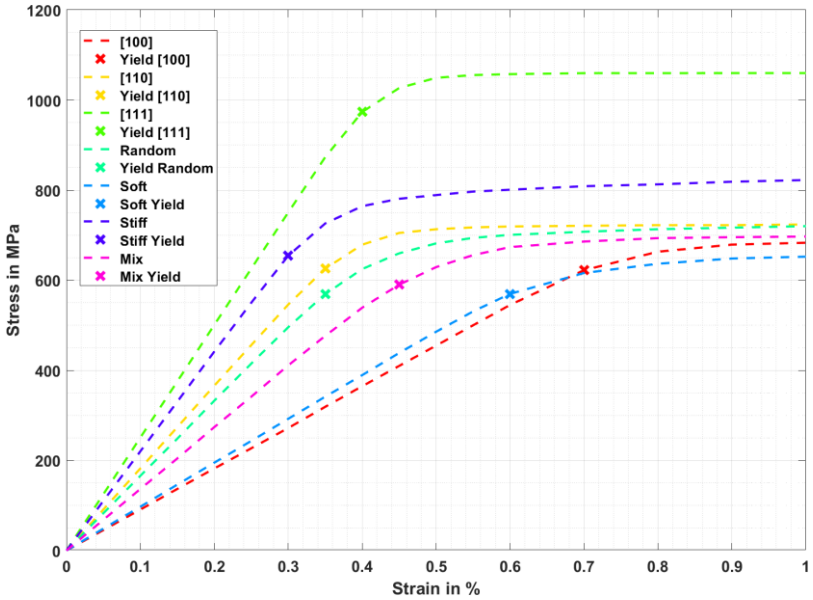

Figure 4. Simulated stress-strain curves for different grain orientation distributions for an INC-738 LC at 850 °C.

The overall stress-strain curves comparison shown in Figure 4 shows a significant scatter within the elastic regions. The detailed results for each curve is listed below:

- For the [100] orientation distribution the lowest Young's moduli of 91.19 GPa can be found. The yield point is reached at 622 MPa with an elastic strain of 0.7 %.
- For the soft orientation distribution, which slightly differs from the [100] orientation distribution (see Figure 3), the Young's moduli is marginal higher with 97.58 GPa. However, yield is distinct lower and reached at 568 MPa and a related elastic strain of 0.6 %.
- Highest Young's moduli is reached for the [111] orientation distribution with 250.45 GPa and yield at 973 MPa with an elastic strain of 0.4 %.
- The stiff orientation distribution reaches yield first, i.e., shows lowest elastic strain compared to all other investigated orientation distributions. Besides a quite high Young's modulus of 220.37 GPa, yield is reached at 0.3% with a yield stress of 655 MPa.
- The [110] orientation distribution as well as the random orientation distribution show same elastic strains at the yield point with 0.35%. But due to slightly higher Young's modulus for the [110] orientation distribution with 182.67 GPa, the yield stress is also slightly higher with 625 MPa.
- In order to consider the influence of random orientation distributions and the resulting scatter, six simulations were statistically evaluated, where the average stress-strain curve is shown in Figure 4. For the random orientation distribution, the Young's modulus is 163.8 ± 4.8 GPa and yield stress is reached at 561.63 ± 15.17 MPa.
- The mix orientation distribution shows a Young's modulus of 136.37 GPa and yields at 590 MPa and 0.45 % total strain.

Figure 5 shows the local elastic strain in the loading direction as well as the equivalent plastic strain for a simulated specimen with a random grain orientation at 1 % total strain (turquoise curve, see Figure 4).

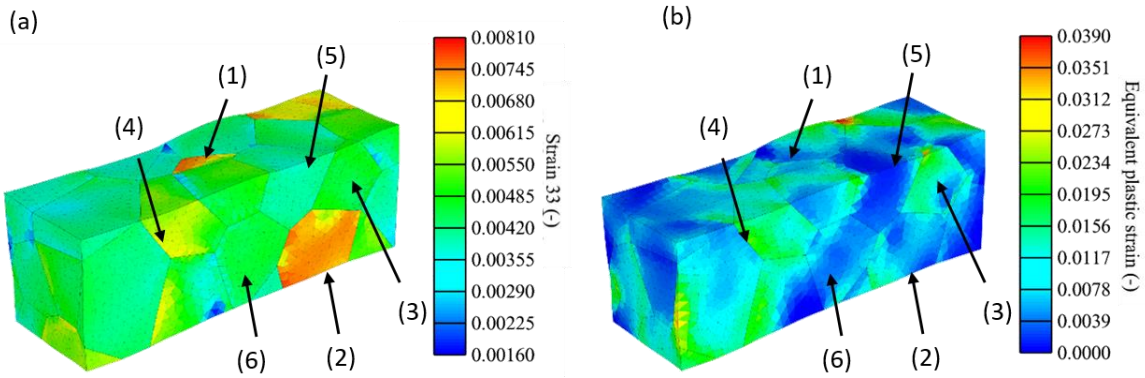

Figure 5. (**a**) Elastic strain S33 in loading direction and (**b**) equivalent plastic strain for a randomly orientated specimen.

The elastic strain distributions in loading direction are inhomogeneous, where some grains show significantly higher elastic strains compared to others. Interestingly, these high elastic strain grains show low equivalent plastic strains as seen at grain (1) and (2) in Figure 5b. Higher plastic strains have been observed in grains that show intermediate elastic strains, as demonstrated by grain (3). Grain (4) shows both, high local elastic strain as well as high equivalent plastic strain, whereas grain (5) and (6) see intermediate elastic strains, but almost negligible equivalent plastic strain. Figure 6 shows the distribution and development of equivalent plastic strain for the specimen shown in Figure 5, at 0.2 %, 0.4 %, 0.6 % and 0.8 % of total strain.

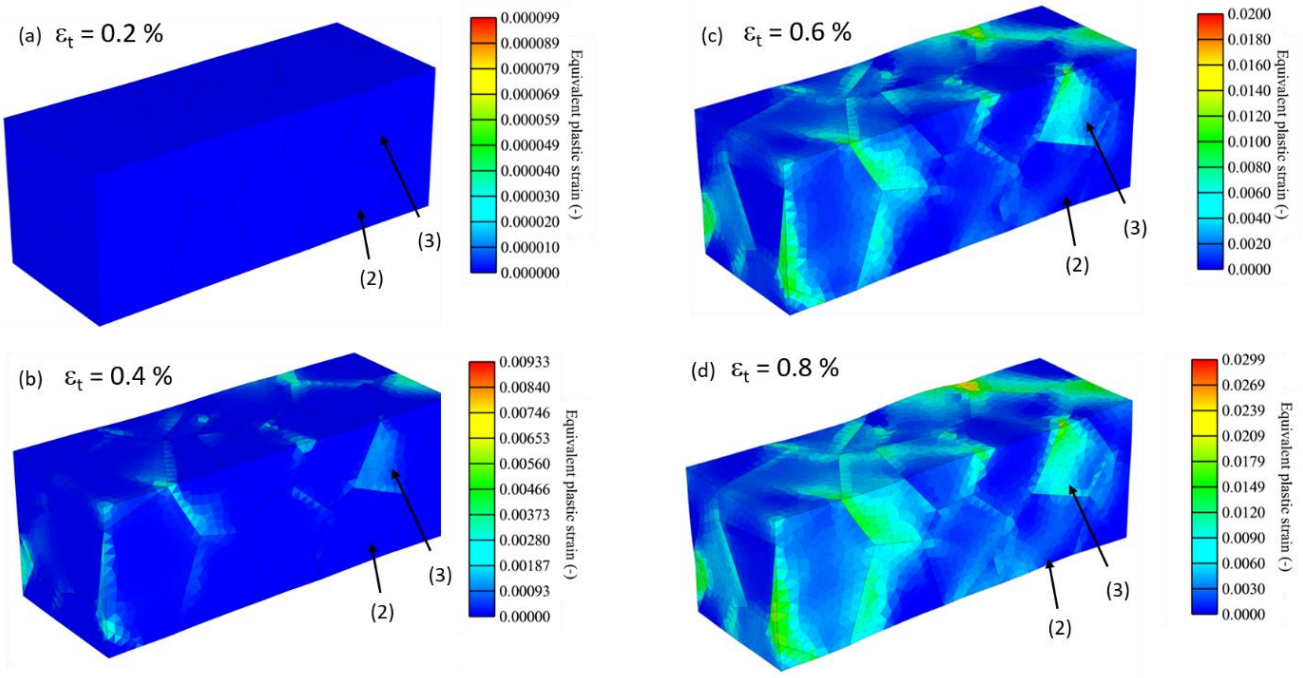

Figure 6. Distribution of equivalent plastic strain under (**a**) 0.2 %, (**b**) 0.4 %, (**c**) 0.6 % and (**d**) 0.8 % total strain for the randomly orientated grain distribution.

For a total strain of 0.2 %, no plastic strain within the whole material can be determined. At a total strain of 0.4 % some plastic deformation can be seen to occur at some grain boundaries. At this strain, the previously discussed grain (2) displays no plastic deformation, whereas grain (3) already does. Plastic deformation continues to increase as the total strain increases to 0.6 % and grain (2) still shows only minor plastic deformation. For a total strain of 0.8 % grain (2) show slightly increased plastic deformation whereas for grain (3) plastic strain is significantly increased.

Figure 7 shows the distribution of elastic strain in the loading direction and the equivalent plastic strain for a simulated specimen with the soft orientation distribution at 1 % of total strain (light blue curve, see Figure 4).

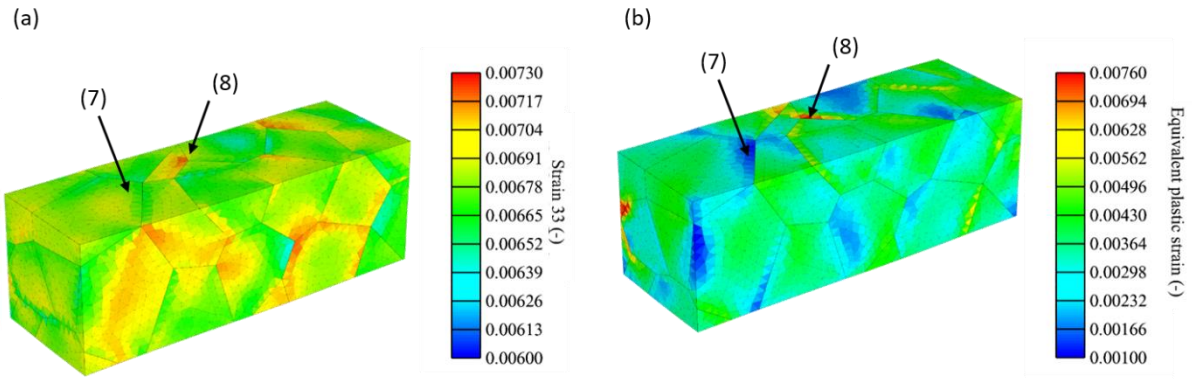

Figure 7. (**a**) Elastic strain S33 in loading direction and (**b**) equivalent plastic strain, for the soft orientated specimen.

The results shown in Figure 7 for a specimen with soft orientation distribution, show a much more homogeneous distribution of high elastic strains within the material (see scale range), compared with the previous shown specimen. This leads to an approximately uniform distribution of equivalent plastic strains with small areas of slightly increased equivalent plastic strain (see grain (8)) or slightly decreased equivalent plastic

strain (see grain (7)). The small deviations arise from similar but not equal grain orientations (see pole figure in Figure 3a).

A contrary behaviour can be seen for the stiff orientation distribution in Figure 8 (see blue curve in Figure 4). The elastic strains are in general much smaller compared to the soft orientation distribution and high values are occasionally located at grain boundaries as the grains (9) shows.

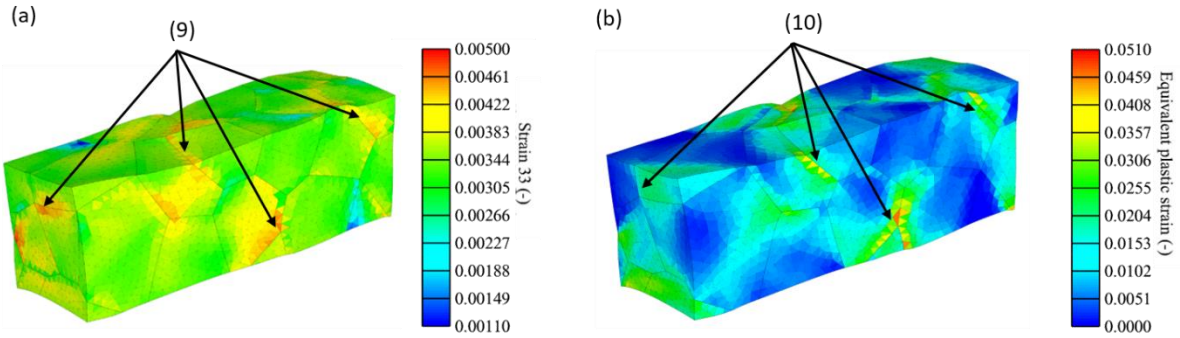

Figure 8. (**a**) Strain S33 and (**b**) equivalent plastic strain in loading direction for the stiff orientated specimen.

According to Figure 8b and the grains indicated with (10), it appears that highest plastic deformations mostly occur close to grain boundaries and decline into the grain. Areas which show high elastic strains also show high equivalent plastic strains. As the simulation also shows, high multi-axial deformation is added to the stiff specimen during a simulated uniaxial test.

Figure 9 shows the results for the mix specimen under a total strain of 1 %. It should be noted here that the first 25 grains have a stiff orientation distribution whereas the last 24 show a soft orientation distribution (if counted from the right).

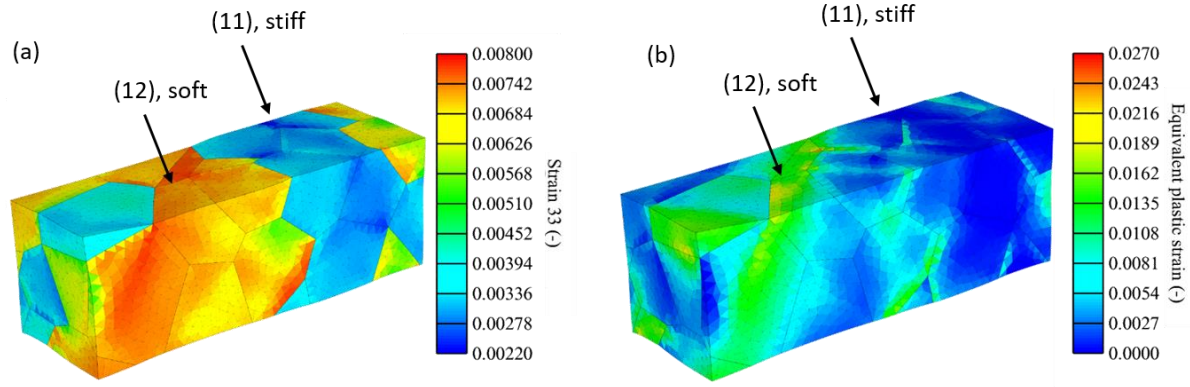

Figure 9. Elastic strain S33 in loading direction (**a**) and equivalent plastic strain (**b**) for the mix orientated specimen.

The elastic strains in the soft part of the specimen (12) are significantly higher compared to the stiff orientated part (11), which is caused by the grain orientation and their associated low Young's moduli. However, the soft part shows significantly larger equivalent plastic strains as compared to the stiff part.

4. Discussion

The stress-strain curves, shown in Figure 4, represent what was already assumed in the $\boldsymbol{E \cdot m}$ model. Even if the [100] and the soft orientation distribution show similar Young's moduli (see Figure 10b), their yielding behaviour is different. This is due to the case that the [100] close orientations show average Schmid factors of 0.412 ± 0.0019, whereas the soft orientation distribution shows distinct higher average value for the Schmid factor of 0.455 ± 0.0036, as Figure 10a represents. The slightly increased Young's moduli together with higher Schmid factors for the soft orientation distribution leads to average $\boldsymbol{E \cdot m}$ values of 43.57 ± 0.023 and thus leads to earlier plastic deformation at the same strains as for the [100] orientation distribution with average $\boldsymbol{E \cdot m}$ values of 37.65 ± 0.1834.

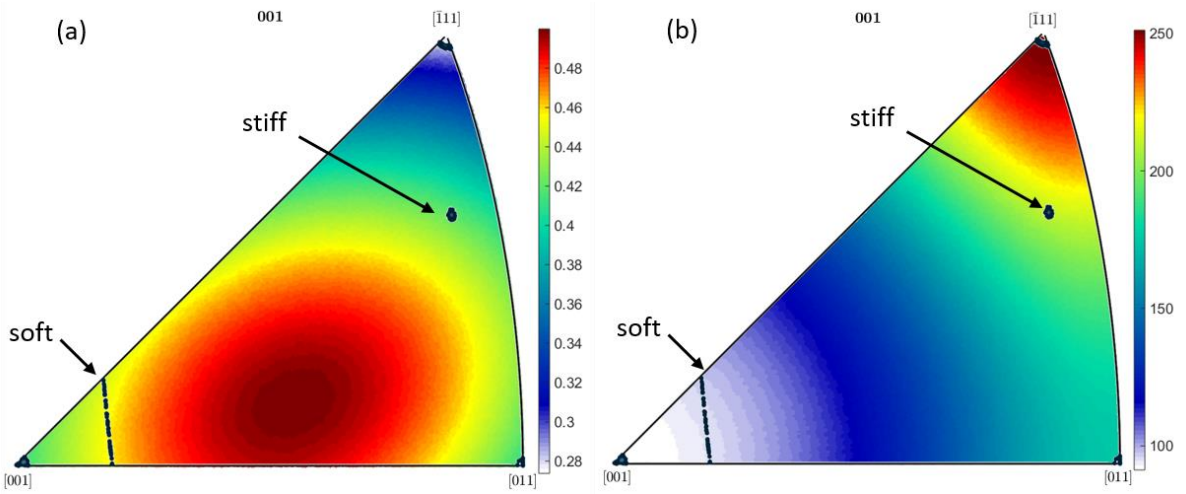

Figure 10. Inverse pole plot of the Schmid factor (**a**), inverse pole plot of the Young's moduli of IN-738 LC at 850 °C (**b**) and the chosen orientation distributions.

Comparing the stiff and the [111] orientations distributions also shows an interesting behaviour. For the [111] orientation the space diagonal of a unit cell of the investigated nickel-based superalloy aligns with the loading direction and shows a global maximum in Young's moduli with about 250 GPa. Despite the fact that the stiff orientation has a lower Young's moduli of 220 GPa it yields at significantly lower strains (see blue curve, Figure 4). Also in this case the Schmid factor distribution is the important factor. For orientations close to the [111] direction, Schmid factor shows a global minimum with average Schmid factors of 0.284 ± 0.0015, whereas the stiff orientation distribution shows average Schmid factors of 0.421 ± 0.0016. However, if both Young's moduli and Schmid factor are considered in combination within the $\boldsymbol{E \cdot m}$ model, it becomes apparent that the stiff orientation distribution leads to a global maximum in $\boldsymbol{E \cdot m}$ with 88.09 ± 0.038 as shown in Figure 3.

Thus, it follows that the stiff orientation distribution globally shows lowest elastic strain, i.e., start to plastic deform as first, compared to other orientation distributions, although this distribution doesn't show maxima in Schmid factor neither in Young's modulus. First as a combination in the $\boldsymbol{E \cdot m}$ model, it becomes obvious why the stiff orientation distribution shows the explained behaviour. A comparison of the stiff orientation distribution and its Schmid factor distribution with 0.421 ± 0.0016 and the soft orientation distribution and its Schmid factor distribution with 0.455 ± 0.0036 also reveal the fact that a higher Schmid factor doesn't necessarily lead to higher shear stresses, as it could possibly be assumed. Moreover, the Young's moduli has also to be considered to make reliable statements about the occurring shear stress within the slip systems.

Since the individual orientations for the distributions [100], [110], [111], stiff and soft are all very close to each other, no large scatter in local mechanical properties were expected and proven by the finite element results. However, for the random orientation distribution, a statistical analysis has been carried out because of a large occurring scatter in local and global mechanical properties (see Figure 5). The following Figure 11 shows the distribution of the random grain orientations for all five simulated specimen within an inverse $\boldsymbol{E} \cdot \boldsymbol{m}$ pole plot; additionally, the grains (1)–(6) from Figure 5 are highlighted.

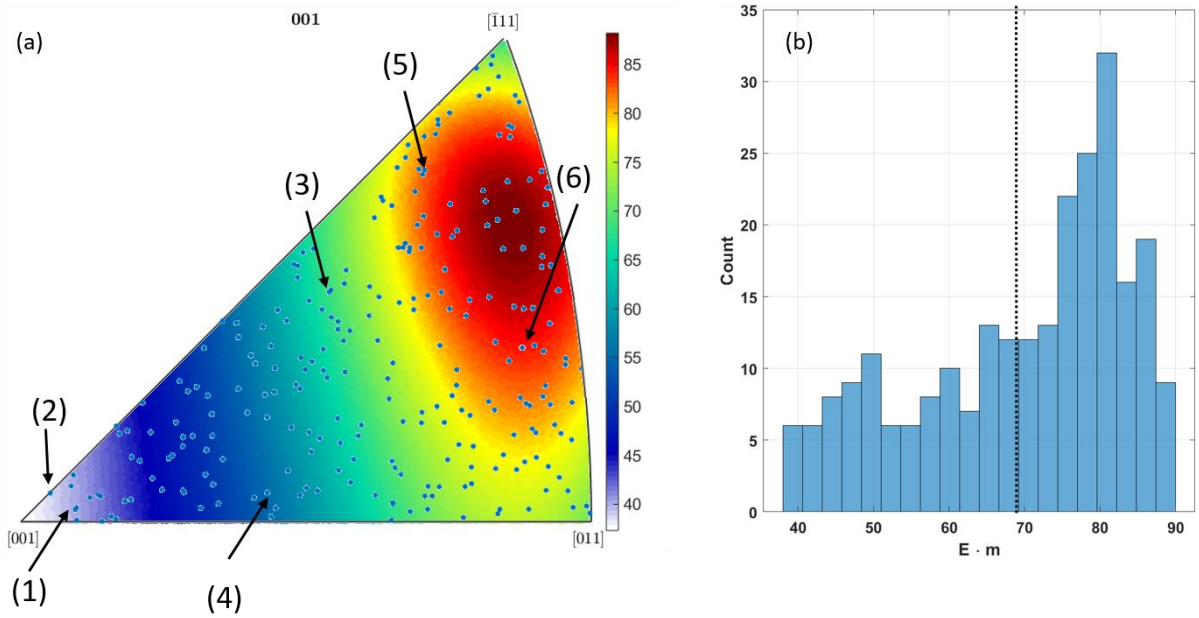

Figure 11. Distribution of random orientations in the inverse $\boldsymbol{E} \cdot \boldsymbol{m}$ plot (**a**) and its histogram (**b**).

It can be clearly seen at the inverse pole plot that the orientations are randomly distributed, whereas on average the $\boldsymbol{E} \cdot \boldsymbol{m}$ value is calculated to 69.57 ± 13.89 (see Figure 11 (b)). The histogram also shows a shift of the distribution to higher $\boldsymbol{E} \cdot \boldsymbol{m}$ values, which underline the fact that for a random orientation, a high $\boldsymbol{E} \cdot \boldsymbol{m}$ value (> 70) is more likely than a low one. It should be noted for the random specimen, since the orientations and therefore the mechanical properties differ over a wide range, the strain distributions also are not homogeneously distributed compared to the specimen where orientation just differs slightly. As grain (2) in Figure 5 shows, large elastic strains in loading direction evolve, but only minor plastic strains are generated. This is caused by its orientation, as Figure 11a shows. The orientation is close to [100] and allows due to lowest $\boldsymbol{E} \cdot \boldsymbol{m}$ values high elastic strains before plastic deformations starts at a total strain of 0.6 %, as the stress-strain curve in Figure 4 shows. In comparison grain (3) has an intermediate $\boldsymbol{E} \cdot \boldsymbol{m}$ value, which leads to lower elastic strains and more equivalent plastic strains. For the mentioned cases of grain (2) and (3) in Figure 5, the $\boldsymbol{E} \cdot \boldsymbol{m}$ approach works well to estimate the onset of plasticity, which is due to the case that both grains show total strains of same magnitude until yield is reached as the following Figure 12a shows.

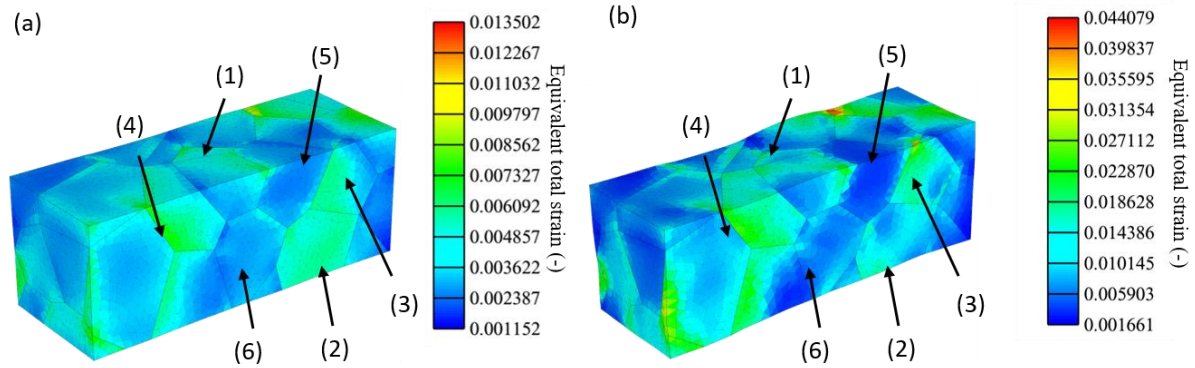

Figure 12. Equivalent total strain for (**a**) 0.4 % global applied total strain and (**b**) 1 % global applied total strain**.**

But within the random orientated specimen, grains appear that show remarkably low total strain, and therefore there is nearly no plastic deformation as grain (5) indicates. Even with an $\boldsymbol{E \cdot m}$ value of 82.16, the amount of strain that is generated within the grain is not sufficient enough to reach yield and to generate plastic deformation, even at a global total strain of 1 %. The same behaviour can be found for grain (6), which has a calculated $\boldsymbol{E \cdot m}$ value of 83.5 but only show low equivalent plastic deformation. It appears that the grains (2) and (3), both with much lower $\boldsymbol{E \cdot m}$ value, generate much more local equivalent total strain as the connected grains (5) and (6). A similar behaviour can be observed in the mix specimen. The stiff part with an average $\boldsymbol{E \cdot m}$ value of 88.1 ± 0.038 shows distinct lower equivalent total strains and therefore lower equivalent plastic strains compared to the soft part with an average $\boldsymbol{E \cdot m}$ of 43.57 ± 0.023. Due to the higher local strains, the soft part of the specimen generates the majority of the plastic deformation. These results lead to the hypothesis that if grains with a low $\boldsymbol{E \cdot m}$ value are interacting with grains with high $\boldsymbol{E \cdot m}$ value, the softer grains will see higher local total strains and therefore more potential plastic deformation compared to stiff grains. This behaviour could already be observed in [9,12] during fatigue testing, where cracks either initiate in grains with high $\boldsymbol{E \cdot m}$ value or in grains with a low $\boldsymbol{E \cdot m}$ value, which are interacting and surrounded with grains with a high $\boldsymbol{E \cdot m}$.

5. Conclusions

The presented work could clearly demonstrate by means of numerical simulations the influences of different grain orientation distributions on the local and global mechanical behaviour of IN-738 LC. It could be shown that grain orientations close to the [100] direction provide lowest Young's moduli and additionally highest elastic strains before yielding. It could be also shown that orientation distributions close to the [111] direction generates highest Young's moduli, but interestingly not the lowest elastic strains before yielding. This could be attributed to lowest Schmid factors associated with the [111] direction. Using the $\boldsymbol{E \cdot m}$ model, which considers both Young's moduli and Schmid factor in dependence of the orientation, it could be found that orientations close to the [$\bar{5}$89] direction show a global maximum in the $\boldsymbol{E \cdot m}$ model and therefore lowest elastic strains before yielding. Since the $\boldsymbol{E \cdot m}$ model is only able to predict the onset of plasticity if a uniform and homogeneous strain distribution is considered, random grain orientation distribution were simulated. Due to a high range of possible mechanical properties of the grains caused by elastic and plastic anisotropies, the total strain distribution is highly inhomogeneous. For regions in the material where the total strain is evenly distributed, the $\boldsymbol{E \cdot m}$ allows for the indication of which grains show plastic deformation first. But, if grains with high and low $\boldsymbol{E \cdot m}$ value interact, most of the total strain is taken by grains with low $\boldsymbol{E \cdot m}$ value (due to low stiffness), which therefore show more plastic deformation compared to surrounding grains with a high $\boldsymbol{E \cdot m}$ value.

The presented results were derived from modeling a specific nickel-based superalloy. But the determined elastic plastic behaviour in dependence of the grain orientation, i.e., the $\boldsymbol{E} \cdot \boldsymbol{m}$ value, can be applied to all cubic fcc metals as long the plastic deformation occurs within the {111}<110] slip systems. Extensions of the model to bcc metals as well as other slip systems are also possible. The shown approach is particularly interesting because almost all metallic materials show an anisotropic elastic behaviour on the microscale. Future investigations should focus on the application of the shown procedure to more complex geometries and multi-axial stress states.

Author Contributions: B.E. wrote the present paper and did the conceptualization and methodology, C.H. and B.E. supervised the numerical modelling conducted by M.H. C.H. and M.H. did the review and editing. All authors have read and agreed to the published version of the manuscript.

Funding: No funding.

Institutional Review Board Statement: Not applicable.

Informed Consent Statement: Not applicable.

Data Availability Statement: Not applicable.

Conflicts of Interest: The authors declare no conflicts of interest.

References

1. Walsh, P.P.; Fletcher, P. *Gas Turbine Performance*; Blackwell Science Ltd: Oxford, UK, 2004.
2. Mäde, L.; Schmitz, S.; Gottschalk, H.; Beck, T. Combined notch and size effect modeling in a local probabilistic approach for LCF. *Comput. Mater. Sci.* **2018**, *142*, 377–388. https://doi.org/10.1016/j.commatsci.2017.10.022.
3. Mäde, L.; Kumar, K.; Schmitz, S.; Gundavarapu, S.; Beck, T. Evaluation of component-similar rotor steel specimens with a local probabilistic approach for LCF. *Fatigue Fract. Eng. Mater. Struct.* **2020**, *43*, 932–946. https://doi.org/10.1111/ffe.13166.
4. Moch, N. From Microscopic Models of Damage Accumulation to the Probability of Failure of Gas Turbines. Ph.D Thesis, Universitätsbibliothek Wuppertal, Wuppertal, Germany, 2019.
5. Rösler, J.; Harders, H.; Bäker, M. *Mechanisches Verhalten der Werkstoffe*; Springer Fachmedien Wiesbaden: Wiesbaden, Germany, 2012; ISBN 978-3-8348-1818-8.
6. Dou, Y.; Luo, H.; Zhang, J. Elastic Properties of FeCr20Ni8Xn (X = Mo, Nb, Ta, Ti, V, W and Zr) Austenitic Stainless Steels: A First Principles Study. *Metals* **2019**, *9*, 145. https://doi.org/10.3390/met9020145.
7. Hasanzadeh, A.; Hamedani, A.; Alahyarizadeh, G.; Minuchehr, A.; Aghaei, M. The role of chromium and nickel on the thermal and mechanical properties of FeNiCr austenitic stainless steels under high pressure and temperature: A molecular dynamics study. *Mol. Simul.* **2019**, *45*, 672–684. https://doi.org/10.1080/08927022.2019.1578357.
8. Schmid, E.; Boas, W. *Plasticity of Crystals with Special Reference to Metals*; F.A. Hughes, USA, 1950.
9. Engel, B. Einfluss der lokalen Kornorientierung und der Korngröße auf das Verformungs- und Ermüdungsverhalten von Nickelbasis Superlegierungen. Ph.D Thesis, Technische Universität Kaiserslautern, Kaiserslautern, Germany, 2019.
10. Seibel, T. Einfluss der Probengröße und der Kornorientierung auf die Lebensdauer einer polykristallinen Ni-Basislegierung bei LCF-Beanspruchung. Ph.D Thesis, Forschungszentrum Jülich, Jülich, Germany, 2014.
11. Schmitz, S.; Seibel, T.; Beck, T.; Rollmann, G.; Krause, R.; Gottschalk, H. A probabilistic model for LCF. *Comput. Mater. Sci.* **2013**, *79*, 584–590. https://doi.org/10.1016/j.commatsci.2013.07.015.
12. Engel, B.; Beck, T.; Moch, N.; Gottschalk, H.; Schmitz, S. Effect of local anisotropy on fatigue crack initiation in a coarse grained nickel-base superalloy. *MATEC Web Conf.* **2018**, *165*, 4004. https://doi.org/10.1051/matecconf/201816504004.
13. Engel, B.; Mäde, L.; Lion, P.; Moch, N.; Gottschalk, H.; Beck, T. Probabilistic Modeling of Slip System-Based Shear Stresses and Fatigue Behavior of Coarse-Grained Ni-Base Superalloy Considering Local Grain Anisotropy and Grain Orientation. *Metals* **2019**, *9*, 813. https://doi.org/10.3390/met9080813.
14. Engel, B.; Beck, T.; Schmitz, S. (Eds.). High temperatue Low Cylce Fatigue of the Ni-base Superallor René80. In Proceedings of the Eighth International Conference on Low Cycle Fatigue (LCF8), Dresden, Dresden, 27–29 June 2017.
15. Engel, B.; Ohneseit, S.; Mäde, L.; Beck, T. Influence of Grain Orientation Distribution on the High Temperature Fatigue Behaviour of Notched Specimen Made of Polycrystalline Nickel-Base Superalloy. *Metals* **2021**, *11*, 731. https://doi.org/10.3390/met11050731.
16. Bayerlein, U.; Sockel, H. Bayerlein, U.; Sockel, H. Determination of single crystal elastic constants from ds- and dr-ni-based superalloys by a new regression method between 20 °C and 1200 °C. *Superalloys* **1992**, 695–704.
17. Tobias, J.; Chlupova, A.; Petrenec, M.; Polak, J. (Eds.). Low Cycle Fatigue and Analysis of the Cyclic Stress-Strain Response in Superalloy Inconel 738LC. In Proceedings of the 18th International Conference of Engineering Mechanics, Svratka, Czech, 14–17 May 2012.

18. Šmíd, M.; Petrenec, M.; Polák, J.; Obrtlík, K.; Chlupová, A. Analysis of the Effective and Internal Cyclic Stress Components in the Inconel Superalloy Fatigued at Elevated Temperature. *AMR* **2011**, *278*, 393–398. https://doi.org/10.4028/www.scientific.net/AMR.278.393.
19. Quey, R.; Dawson, P.R.; Barbe, F. Large-scale 3D random polycrystals for the finite element method: Generation, meshing and remeshing. *Comput. Methods Appl. Mech. Eng.* **2011**, *200*, 1729–1745. https://doi.org/10.1016/j.cma.2011.01.002.
20. Quey, R.; Renversade, L. Optimal polyhedral description of 3D polycrystals: Method and application to statistical and synchrotron X-ray diffraction data. *Comput. Methods Appl. Mech. Eng.* **2018**, *330*, 308–333. https://doi.org/10.1016/j.cma.2017.10.029.
21. Dawson, P.R.; Boyce, D.E. FEpX—Finite Element Polycrystals: Theory, Finite Element Formulation, Numerical Implementation and Illustrative Examples, 4/13/2015. Available online: http://arxiv.org/pdf/1504.03296v1 (accessed on 12.01.201).
22. Kasemer, M.; Falkinger, G.; Roters, F. A numerical study of the influence of crystal plasticity modeling parameters on the plastic anisotropy of rolled aluminum sheet. *Model. Simul. Mater. Sci. Eng.* **2020**, *28*, 85005. https://doi.org/10.1088/1361-651X/abb8e2.
23. Turkmen, H.S.; Miller, M.P.; Dawson, P.R.; Moosbrugger, J.C. A Slip-Based Model for Strength Evolution During Cyclic Loading. *J. Eng. Mater. Technol.* **2004**, *126*, 329–338. https://doi.org/10.1115/1.1789967.
24. Lin, R.C.; Betten, J.; Brocks, W. Modeling of finite strain viscoplasticity based on the logarithmic corotational description. *Arch. Appl. Mech.* **2006**, *75*, 693–708. https://doi.org/10.1007/s00419-006-0044-6.